PAPER • OPEN ACCESS

Topological aspects of multi-*k* antiferromagnetism in cubic rare-earth compounds

To cite this article: W Simeth *et al* 2024 *J. Phys.: Condens. Matter* **36** 215602

View the article online for updates and enhancements.

Topological aspects of multi-*k* antiferromagnetism in cubic rare-earth compounds

W Simeth[1,2] ⓘ**, M C Rahn**[1,3] ⓘ**, A Bauer**[1,4] ⓘ**, M Meven**[5,6] ⓘ **and C Pfleiderer**[1,4,7,8,*] ⓘ

[1] Physik-Department, Technical University of Munich, D-85748 Garching, Germany

[2] Paul Scherrer Institut, Forschungsstrasse 111, CH-5232 Villigen, Switzerland

[3] Institute for Solid State and Materials Physics, Technical University of Dresden, D-01062 Dresden, Germany

[4] Centre for Quantum Engineering (ZQE), Technical University of Munich, D-85748 Garching, Germany

[5] Forschungszentrum Jülich GmbH, Jülich Centre for Neutron Science (JCNS) at Heinz Maier-Leibnitz Zentrum (MLZ), D-85748 Garching, Germany

[6] Institut für Kristallographie, RWTH Aachen, D-52056 Aachen, Germany

[7] Munich Center for Quantum Science and Technology (MCQST), Technical University of Munich, D-85748 Garching, Germany

[8] Heinz Maier-Leibnitz Zentrum (MLZ), Technical University of Munich, D-85748 Garching, Germany

E-mail: christian.pfleiderer@tum.de

CrossMark

Abstract

We advertise rare-earth intermetallics with high-symmetry crystal structures and competing interactions as a possible materials platform hosting spin structures with non-trivial topological properties. Focusing on the series of cubic RCu compounds, where $R =$ Ho, Er, Tm, the bulk properties of these systems display exceptionally rich magnetic phase diagrams hosting an abundance of different phase pockets characteristic of antiferromagnetic order in the presence of delicately balanced interactions. The electrical transport properties exhibit large anomalous contributions suggestive of topologically non-trivial winding in the electronic and magnetic structures. Neutron diffraction identifies spontaneous long-range magnetic order in terms of commensurate and incommensurate variations of $(\pi\pi0)$ antiferromagnetism with the possibility for various multi-$\boldsymbol{k}$ configurations. Motivated by general trends in these materials, we discuss the possible existence of topologically non-trivial winding in real and reciprocal space in the class of RCu compounds including antiferromagnetic skyrmion lattices. Putatively bringing together different limits of non-trivial topological winding in the same material, the combination of properties in RCu systems promises access to advanced functionalities.

Keywords: antiferromagnetism, Skyrmion lattice, topological spin textures

1. Introduction

In recent years, great interest developed in the use of complex magnetic and the associated electronic properties for spintronics and nano-electronics devices, as well as neuromorphic computing, and related applications [1–7]. Complex magnetic modulations with multiple wave vectors, identified in a rapidly growing number of materials, are at the center of these developments. Such magnetic structures are also referred to as magnetic multi-k states—a notion that dates back at least to the 1970s, when it was used to describe the magnetic modulations in materials such as Nd [8] or $CeAl_2$ [9]. In large parts, recent discoveries with multi-k states at their center were motivated by the search for topologically nontrivial electronic or magnetic states.

To date, the perhaps most intensively studied class of bulk compounds exhibiting topologically nontrivial order are the cubic chiral magnets crystallizing in space group $P2_13$, namely MnSi, $Fe_xCo_{1-x}Si$, FeGe, Cu_2OSeO_3, and related compounds [10]. As illustrated in figure 1, a trigonal lattice of skyrmions is observed in a phase pocket in finite magnetic field, associated with a characteristic sixfold-symmetric pattern in small-angle neutron scattering [11]. At low temperatures, the skyrmion lattice may prevail as a metastable state [10], its arrangement may change, and an additional skyrmion state may form independently [17–19]. In recent years, similar magnetic structures have been reported to exist in a wide range of bulk materials. As shown in figures 1(a2)–(d), examples include skyrmion lattice order in GaV_4S_8 [20], Gd_2PdSi_3 [21], $Gd_3Ru_4Al_{12}$ [22], and $GdRu_2Si_2$ [12], meron–antimeron lattices in $Co_8Zn_9Mn_3$ [13] and CeAlGe [14], monopole–antimonopole lattices in MnGe [15], or fractionalized antiferromagnetic skyrmion lattice in $MnSc_2S_4$ [16]. In addition to these bulk materials, topologically nontrivial magnetic textures have also been reported in thin-film systems in which interfacial Dzyaloshinskii–Moriya interactions are important [10].

A simple tool to search for topologically nontrivial properties in the electronic and magnetic structure are non-vanishing Berry phase contributions in the transport properties [23], with the topological Hall effect in the skyrmion lattice of chiral magnets as an early example [24]. In chiral magnets, these phenomena are extremely well understood on the level of mean-field theory. However, emergent transport phenomena are also used as an indicator for topological magnetic order in rare-earth compounds [21, 22], requiring careful consideration of the coupling between conduction electrons and rare-earth moments [25]. On a similar note, microscopic studies of the electronic and magnetic order require great care. For instance, when using scattering techniques one of the key experimental tasks concerns discrimination of single-domain multi-k states from multi-domain single-k states.

Rare-earth intermetallics with high-symmetric crystal structures represent a class of compounds that was found to exhibit multi-k antiferromagnetic order long ago [26–30]. Despite this long history, these systems so far have not been considered in the search for phenomena associated with nontrivial topological winding. In these compounds, partially filled rare-earth 4f orbitals typically possess a small overlap resulting in vanishingly small direct exchange [31]. Interactions between the 4f moments are instead mediated indirectly via conduction bands and spin–orbit coupling [32–34]. In competition with magnetocrystalline anisotropies and quadrupolar degrees of freedom, rich magnetic phase diagrams emerge supporting various antiferromagnetic forms of order [35–42]. However, these studies predated recent research on the topological properties of magnetic materials motivating to revisit this these systems.

In this paper, we consider selected properties of the class of cubic rare-earth copper compounds, RCu (R = Gd, Tb, Dy, Ho, Er, Tm) that suggest the putative existence of non-trivial topological properties in this class of materials. Table 1 summarizes some of early results on the magnetic structures observed in these systems. Shown in figure 2(a) is the centrosymmetric cubic CsCl crystal structure with space group $Pm\bar{3}m$. Below the Néel temperature T_N, antiferromagnetic order of the rare-earth moments stabilizes. When increasing the atomic number Z from 64 in gadolinium to 69 in thulium, the Néel temperature decreases by a factor of 20, while the lattice constant a decreases by about 3%, as shown in figure 2(b).

Within the parameter range studied, all RCu compounds have been found to exhibit $(\pi\pi0)$ antiferromagnetic order, comprising long-wavelength commensurate and incommensurate superstructures around $k \approx (\frac{1}{2}, \frac{1}{2}, 0)$, i.e. the M point of the Brillouin zone. The ground state at low temperatures and zero magnetic field is reported to be commensurate with $k = (^1/_2, ^1/_2, 0)$, with single-k, double-k, or triple-k magnetic structures being allowed in the high-symmetry crystal structure. A triple-k structure was identified for instance in DyCu [39, 40, 51, 52], while additional incommensurate log-wavelength superstructures, such as those reported in TmCu and ErCu, were exclusively considered to be single-k.

The focus of our paper concerns the possible topological character of such single-k and multi-k antiferromagnetic structures. We motivate these considerations in terms of a few selected experimental observations, noting that the full experimental studies of different materials are well beyond the scope of our paper. We begin in section 2.1 with the magnetic phase diagrams of HoCu, ErCu, and TmCu for field along $\langle 111 \rangle$ as inferred from the magnetic AC susceptibility. Typical for this class of materials and all field directions is an abundance of field-induced transitions with an exceptionally rich and complex sequence of phase pockets. This underscores the presence of a fragile balance of interactions comprising exchange, spin–orbit coupling, crystal fields, and f-electron itinerancy. As illustrated for the case of TmCu in section 2.2, measurements of the electrical transport properties in all of these materials exhibit an anomalous field dependence that does not scale with the magnetization, suggestive of non-vanishing Berry phase contributions in real and reciprocal space. Finally, as illustrated in section 2.3 for HoCu at zero
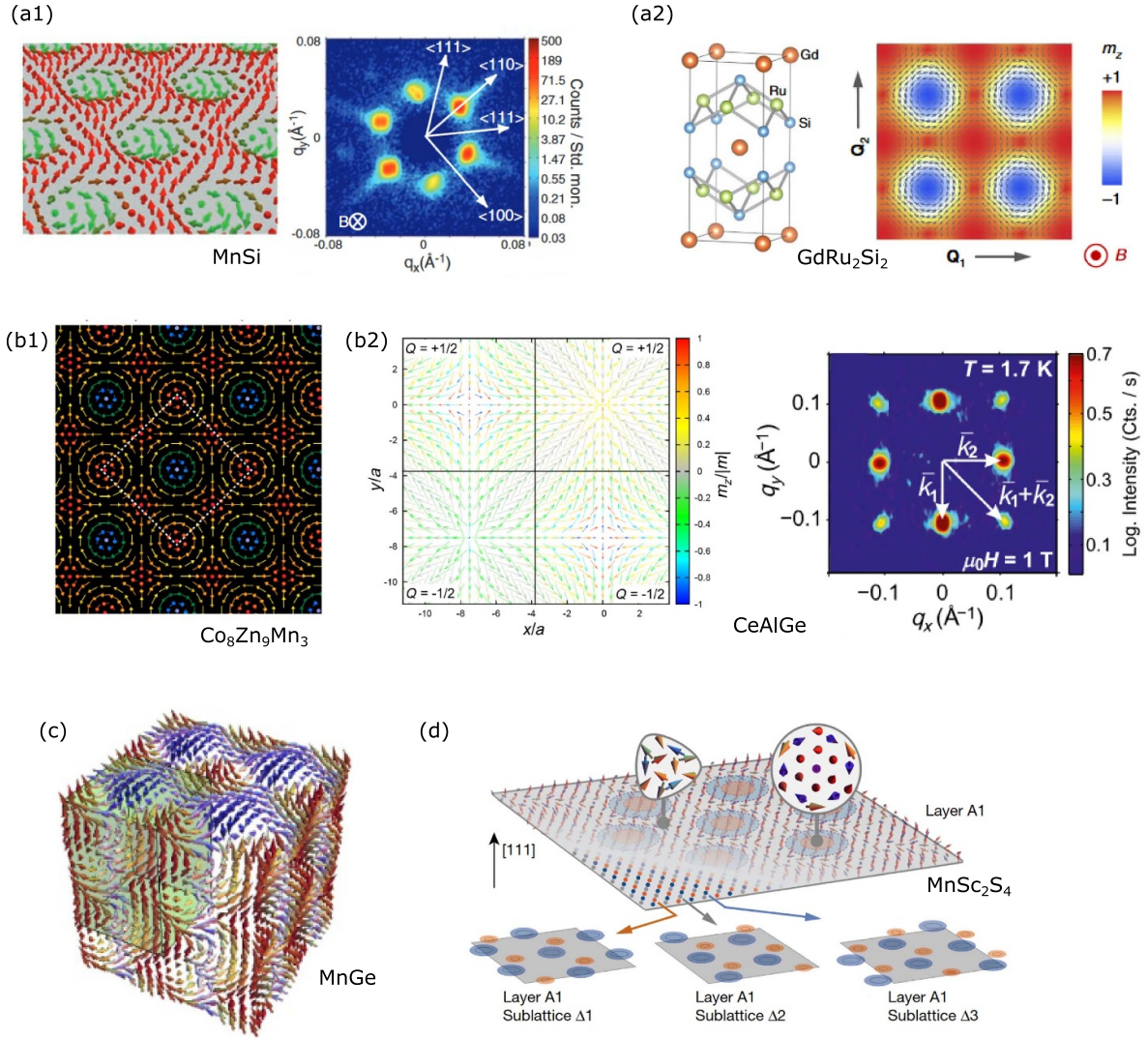
Figure 1. Survey of materials for which magnetic multi-*k* states with nontrivial topology have been reported. (a1) Trigonal skyrmion lattice in the cubic chiral magnet MnSi. Left: visualization of the magnetic texture in the plane perpendicular to the magnetic field. Right: typical small-angle neutron scattering pattern [11]. (a2) Nanometric square skyrmion lattice in the centrosymmetric tetragonal magnet $GdRu_2Si_2$. Left: crystal structure. Right: arrangement of the magnetic moments in the basal plane [12]. (b1) Meron–antimeron lattice in chiral magnet $Co_8Zn_9Mn_3$ [13]. (b2) Meron–antimeron lattice in the polar tetragonal magnet CeAlGe. Left: arrangement of the magnetic moments in the basal plane. Right: typical small-angle neutron scattering pattern [14]. (c) Three-dimensional monopole–antimonopole in cubic MnGe [15]. (d) Fractionalized antiferromagnetic skyrmion lattice in layered $MnSc_2S_4$ [16].

Table 1. Overview of simple cubic rare-earth intermetallics that were reported to host variations of $(\pi\pi0)$-type magnetic order with propagation vectors associated with the $\boldsymbol{Q}$-positions $(1/2, 1/2, 0)$ or $(1/2 - \delta, 1/2, 0)$.

Structure type	Commensurate, $\boldsymbol{k} \in \langle 1/2, 1/2, 0 \rangle$	Incommensurate, $\boldsymbol{k} \in \left\{ (1/2 - \boldsymbol{\delta}, 1/2, 0) \right\}$
CsCl	PrAg [43, 44], NdAg [45], TbAg [46], DyAg [47], ErAg [48], GdCu [49], TbCu [46], HoCu [50], TmCu [50], ErCu [50], DyCu [39, 40, 51, 52]	HoAg [53], ErAg [48], TmAg [53], ErCu [50], TmCu [50]
$AuCu_3$	NdIn₃ [41], DyIn₃ [42], TmGa₃ [54], TbIn₃ [55], HoIn₃ [55]	ErGa₃ [56]

magnetic field, single-crystal neutron diffraction data reveal the existence of antiferromagnetic structures that combine short-wavelength commensurate order with incommensurate superstructures.

Taken together, these experimental appetizers motivate a dedicated study of the topological character of such magnetic structures. This analysis forms the main part of our paper, presented in section 3. We begin with a detailed discussion
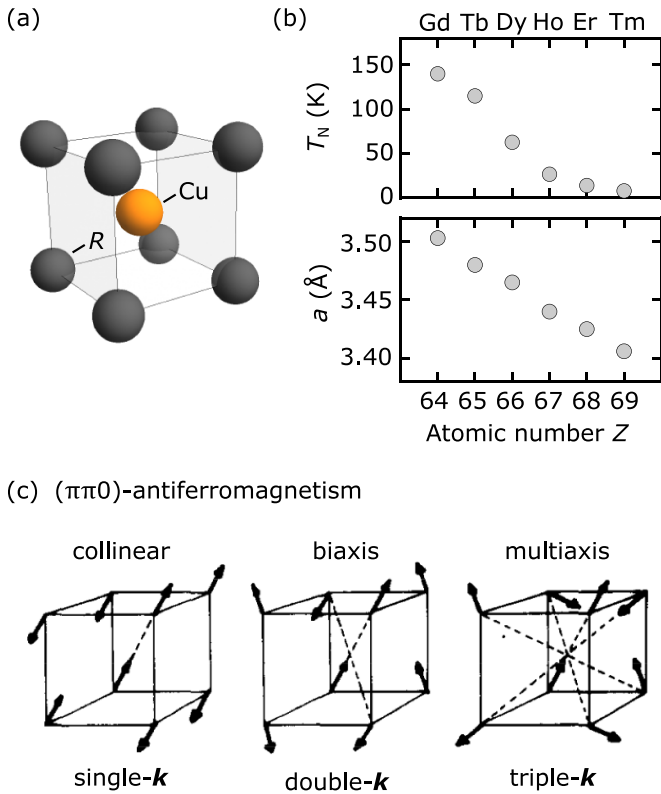
(a)

(b)

(c) (ππ0)-antiferromagnetism

Figure 2. Overview of the magnetic properties of cubic rare-earth copper compounds *R*Cu. (a) CsCl crystal structure, space group *Pm3̄m*. (b) Néel temperature T_N (top) and room-temperature lattice constant *a* (bottom) as a function of the atomic number *Z* of the rare-earth element. Note that GdCu and TbCu undergo martensitic transitions to orthorhombic phases at low temperatures [57]. (c) Illustration of potential (ππ0) antiferromagnetic order composed of one, two, or three commensurate wave vectors *k*, suggested as possible ground states of HoCu. Reprinted from [50], Copyright (1980), with permission from Elsevier.

of the commensurate multi-*k* states in section 3.1, which may be viewed in terms of a topological band structure comprising monopoles and antimonopoles in reciprocal space. In comparison, the incommensurate multi-*k* superstructure, addressed in section 3.2, may be interpreted in terms of topologically non-trivial, long-wavelength magnetic textures in real space, such as an antiferromagnetic skyrmion lattice. Our paper concludes in section 4 with a summary and a brief outline of the work program our considerations motivate, which is needed to develop a comprehensive understanding of cubic rare-earth intermetallics.

2. Typical experimental signatures

2.1. Magnetic phase diagrams

Shown in figure 3 are the phase diagrams of HoCu, ErCu, and TmCu under magnetic fields applied parallel to ⟨111⟩. The phase diagrams were derived from the AC susceptibility [58–61] measured on large single crystals grown by means of the optical floating-zone technique [62, 63]. Marked in

red are extrema and points of inflection as recorded at an excitation frequency of 911 Hz and excitation amplitude of 1 mT. Characteristic of a complex antiferromagnetic ground state, the phase diagrams on a purely phenomenological level suggest the formation of a large number of phase transitions and cross-over phenomena before the field-polarized regime is reached. As a function of increasing *Z*, i.e. decreasing lattice spacing and single-ion moment when going from Ho to Er to Tm, the onset of the field-polarized state and the ordering temperature T_N decrease. Similarly, the number of magnetic phase pockets decreases across the series. Nonetheless, the mere complexity of the phase diagrams raises the question for the nature of the microscopic magnetic and electronic structure and its possible topological character.

2.2. Electrical transport properties

The electrical transport properties of the series of RCu compounds, quite generically, display a complex magnetic field dependence [58, 61]. Typical behavior may be illustrated for TmCu, where the comparatively small number of field-induced transitions and the low critical field of the field-polarized state allows direct comparison of the transport properties with the magnetization deep into the field-polarized state. As shown in figure 4(a) for $H \parallel \langle 111 \rangle$, corresponding to the phase diagram shown in figure 3(c), the magnetization of TmCu at a low temperature of 2 K is dominated by two step-like transitions at $H_1 = 4.0\,\text{T}$ and $H_2 = 6.7\,\text{T}$, before entering the field-polarized state slightly above $H_c = 9.0\,\text{T}$. Further signatures denoted in the phase diagram may only be seen in the AC susceptibility.

In the field-polarized state for $H > H_c$, the resistivity ρ_{xx}, shown in figure 4(b), increases monotonically with $M(H)$ which is reminiscent of the transverse magnetoresistance observed in conventional ferromagnets. In comparison, between the transition at H_1 and below the onset of the field-polarized state at H_c, the resistivity $\rho_{xx}(H)$ displays an additional contribution highlighted in blue shading. As this additional contribution may reflect any combination of scattering by the magnetic structure and magnetic textures, as well as changes of the electronic structure, its unambiguous identification is beyond the scope of our paper.

Similar to the resistivity $\rho_{xx}(H)$, the Hall resistivity $\rho_{xy}(H)$ shown in figure 4(c), displays essentially a linear dependence in the field-polarized state above H_c. Below H_c, a strongly non-monotonic field dependence is observed, including a change of sign. Notably, the exceptional magnitude of these contributions (purple shading) is remarkable in its own right. It is instructive to assess the Hall resistivity in the conventional way, considering three main contributions, namely

$$\rho_{xy}(H) = R_0\,\mu_0 H + S_A\,\mu_0\,\rho_{xx}^2 M(H) + \Delta\rho_{xy}(H)\,. \quad (1)$$

Here, the first term describes the normal Hall effect which is linear under applied magnetic field, while the second term represents the intrinsic anomalous Hall effect that is linear in the
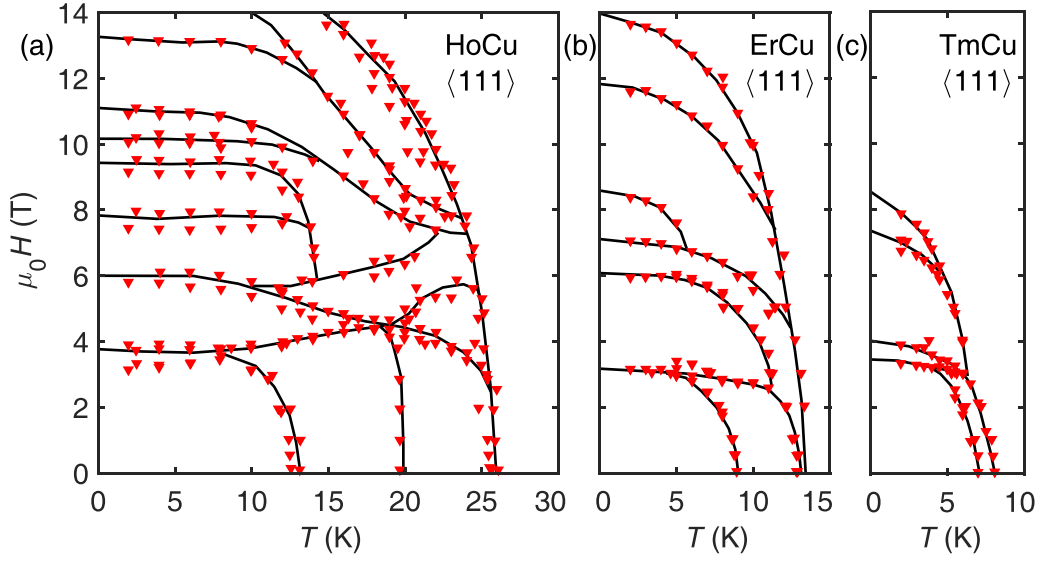
Figure 3. Magnetic phase diagrams of HoCu, ErCu, and TmCu for magnetic field $H \parallel \langle 111 \rangle$. Marked in red are maxima and points of inflection observed in the AC susceptibility. Lines are guides to the eye.
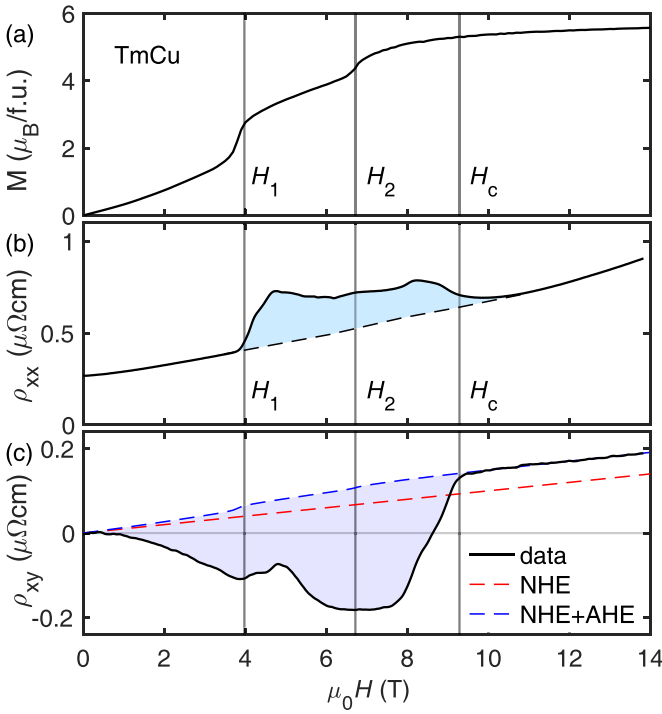

Figure 4. Magnetization and electrical transport properties of TmCu at $T = 2\,\mathrm{K}$ for magnetic field along $\langle 111 \rangle$. (a) Magnetization as a function of magnetic field, where two dominant step-like transitions at $H_1 = 4.0\,\mathrm{T}$ and $H_2 = 6.7\,\mathrm{T}$ are followed by the onset of the field-polarized state slightly above $H_c = 9.0\,\mathrm{T}$. (b) Electrical resistivity ρ_{xx}, featuring a non-monotonic contribution between H_1 and H_c. (c) Hall resistivity ρ_{xy} of TmCu. Dashed lines represent normal and anomalous Hall contributions denoted NHE and AHE, respectively, as matched to the field-polarized state above H_c. An exceptionally large non-monotonic contribution to ρ_{xy} is highlighted by purple shading. This contribution provides putative evidence of non-trivial topology.

magnetization and the resistivity squared. The third term vanishes in the spin-polarized state and is usually attributed to the emergence of additional Berry phase contributions in the presence of magnetic order.

Assuming that the parameter S_A does not change across the complex magnetic phase diagram, the Hall resistivity $\rho_{xy}(H)$ in the field-polarized state is dominated by a normal Hall contribution (NHE) and a small anomalous Hall contribution (AHE) as denoted in figure 4(c). In turn, the anomalous contribution in the resistivity ρ_{xx} between H_1 and the onset of the field-polarized state at H_c is barely noticeable as compared to the non-monotonic part of the Hall resistivity $\rho_{xy}(H)$. This observation underscores the potential presence of a combination of different topological contributions in the transport properties and motivates closer inspection of the magnetic structure presented in the next section.

2.3. Neutron scattering

Typical key characteristics of the magnetic structures in the class of RCu systems may be illustrated by means of HoCu at zero field, featuring commensurate short-wavelength antiferromagnetism as well as incommensurate superstructures. Data were recorded at the single-crystal diffractometer HEiDi at FRM-II [64] in rocking scans with respect to the reciprocal lattice position $\boldsymbol{Q} = (\frac{3}{2}, \frac{3}{2}, 1) + \Delta \boldsymbol{Q}$. As shown in figure 5, the scattering intensity in HoCo at zero magnetic field exhibits three different momentum dependencies with increasing temperature denoted I, II, and III, consistent with the three antiferromagnetic phases observed in the bulk properties. At 2.3 K, the lowest temperatures studied, HoCu displays short-wavelength commensurate $(\pi\pi0)$ antiferromagnetism with wave-vectors forming a star $\{(^1/_2, ^1/_2, 0)\}$, frequently
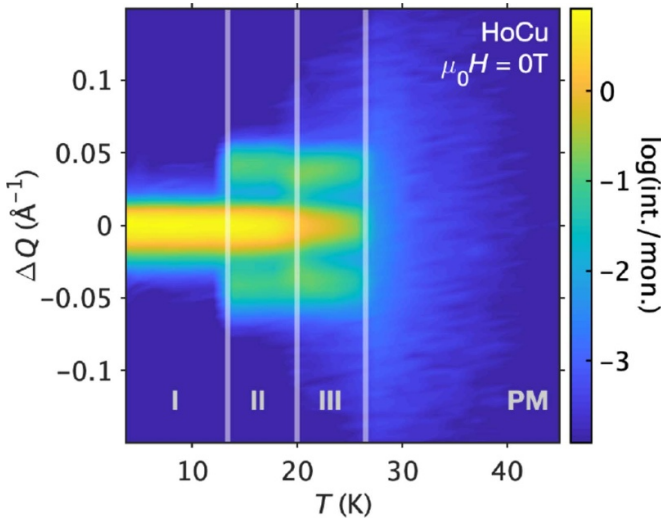
Figure 5. Magnetic neutron diffraction intensity as a function of temperature in HoCu at zero magnetic field. Three phases denoted I, II and III may be distinguished, reflecting commensurate antiferromagnetism in phase I, with an additional incommensurate superstructure in phases II and III.

also denoted $\langle 1/2, 1/2, 0 \rangle$. Further, at intermediate temperatures when entering phases II and III the scattering intensity is characteristic of incommensurate ordering vectors $\{(1/2 - \delta, 1/2, 0)\}$ with $\delta \approx 0.02$ r.l.u. These scattering intensities correspond to a long-wavelength superstructure of the short-wavelength commensurate antiferromagnetic order observed in phase I.

The incommensurate propagation vectors observed in phases II and III are reminiscent of the antiferromagnetic order reported in the large class of cubic rare-earth intermetallics summarized in table 1. While some of the commensurate states have been considered as candidates of short-wavelength multi-$\mathbf{k}$ order, it is interesting to note that the components defining the incommensurate superstructures, $\{(1/2 - \delta, 1/2, 0)\}$, may represent long-wavelength multi-$\mathbf{k}$ modulated states in their own right. We limit the discussion of the magnetic structures in HoCu, presented in the following, to phases I and II, since they permit to address the topological character in two opposing limits. Although in both phases magnetic structure refinements and polarized neutron diffraction may be accounted for by relatively simple collinear forms of antiferromagnetic order, a large set of antiferromagnetic multi-$\mathbf{k}$ states with non-trivial topological properties exists, some of which may ultimately turn out to be the magnetic ground states.

Comprehensive neutron diffraction experiments in HoCu, ErCu, and TmCu under zero and applied magnetic fields at various beam-lines [61, 64–72], which we will report elsewhere, highlight that the characteristics observed in HoCu at zero field are generic for all materials and their magnetic phase diagrams. The combination of various state-of-the-art neutron scattering methods including spherical polarimetry permits us to distinguish between arrangements of magnetic moments with equivalent structure factors [73, 74], as well as between multi-domain single-$\mathbf{k}$ and single-domain multi-$\mathbf{k}$ forms of

order, tracking higher-order magnetic Bragg components (see also [75–77]). These results motivate the theoretical considerations of the topological properties reported in the next section.

3. Theoretical considerations of the topological properties

For the considerations presented in the following, we assume certain plausible choices of the irreducible representation of the magnetic structures. Establishing these irreducible representation for a given material requires magnetic structure refinements by means of high-resolution as well as polarized single-crystal neutron diffraction. In addition, experimental studies are required that permit to distinguish single-domain multi-$\mathbf{k}$ from multi-domain single-$\mathbf{k}$ behavior. This may be achieved, for instance, by means of uniaxial stress or magnetic fields applied in carefully selected orientations breaking certain symmetries. The complexity of the required experimental work places it beyond the scope of the present study. Instead, we focus on the discussion of possible forms of multi-$\mathbf{k}$ magnetic order and their potential for non-trivial topology.

3.1. Phase I of HoCu: commensurate order

For the purpose of the discussion presented in the following, we note that the magnetic structure in phase I of HoCu is consistent with the irreducible representation Γ_9 of the *M* point in space group $Pm\bar{3}m$ [78]. In particular, the magnetic Fourier components propagated by a vector of the star $\langle 1/2, 1/2, 0 \rangle$ are restricted to lie within the plane that is perpendicular to the ferromagnetically coupled $\langle 100 \rangle$ bond of the respective propagation. The orientation of the corresponding arms $\mathbf{k}_{c,1} = (\frac{1}{2}, \frac{1}{2}, 0)$, $\mathbf{k}_{c,2} = (0, \frac{1}{2}, \frac{1}{2})$, and $\mathbf{k}_{c,3} = (\frac{1}{2}, 0, \frac{1}{2})$ is illustrated in figure 6(a), where the magnetic ground state may involve any number of these components.

Presented in figures 6(b)–(d) are examples of single-$\mathbf{k}$, double-$\mathbf{k}$, and triple-$\mathbf{k}$ types of order consistent with the information available about the magnetic structure [79]. Without further constraints, an infinite number of such Γ_9 structures exists, which cannot be distinguished using unpolarized single-crystal neutron diffraction at zero magnetic field. Careful analysis of neutron diffraction recorded under applied magnetic field may then establish that structure t1 shown in figure 6(d) may be the correct solution of phase I.

It is therefore instructive to discuss the properties of t1 in further detail. Namely, the topological properties of the triple-$\mathbf{k}$ state t1 cannot emerge from structures with fewer wave vectors. Unlike the single-$\mathbf{k}$ state representing a collinear structure, and the double-$\mathbf{k}$ state representing a noncollinear coplanar structure, the triple-$\mathbf{k}$ state corresponds to a noncoplanar texture of magnetic moments with finite scalar spin chiralities $\sim \mathbf{M}_i \cdot (\mathbf{M}_j \times \mathbf{M}_l)$ [80]. As a possible account of electrical transport properties such as those observed in TmCu, such spin chiralities may result in real-space Berry phases and anomalous Hall contributions that are not proportional to the net magnetization $M(H)$ [23].
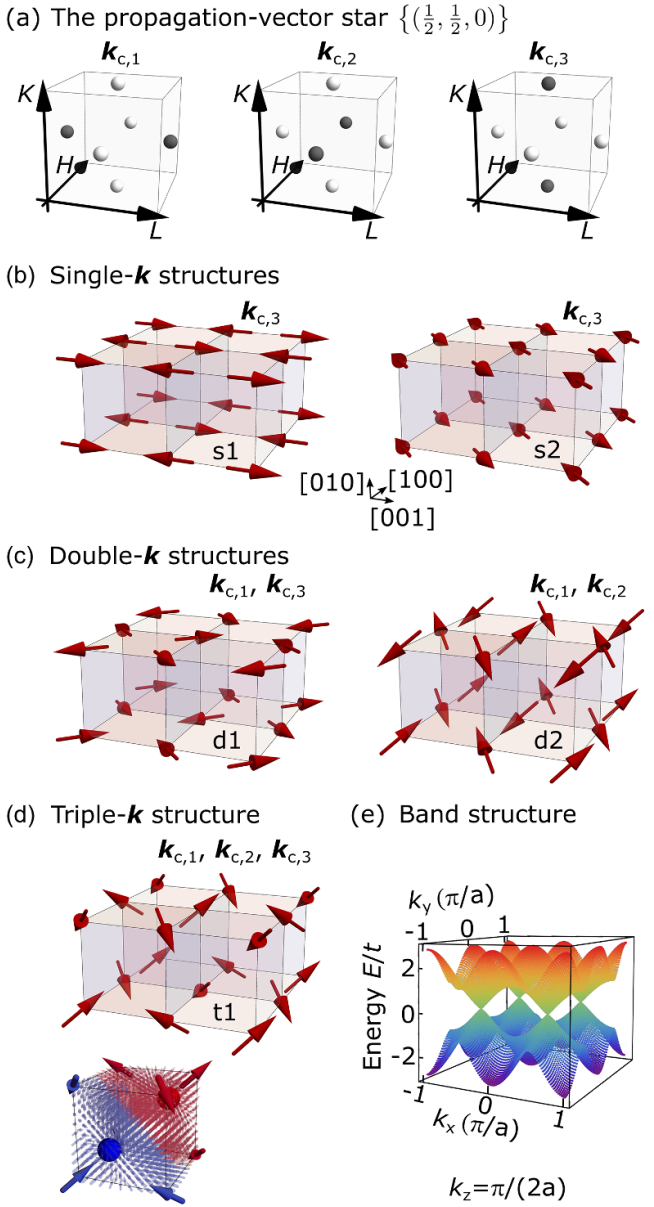
(a) The propagation-vector star $\{(\frac{1}{2},\frac{1}{2},0)\}$

(b) Single-k structures

(c) Double-k structures

(d) Triple-k structure

(e) Band structure

$k_z = \pi/(2a)$

Figure 6. Magnetic structure consistent with phase I in HoCu. The magnetic ground state represents a commensurate $(\pi\pi0)$ antiferromagnet that corresponds to the irreducible representation Γ_9. (a) Reciprocal space illustration in the Brillouin zone of the three arms of the star of propagation vectors $\langle 1/2, 1/2, 0\rangle$. In principle, the wave vectors may form single-k, double-k, or triple-k structures. (b)–(d) Real space examples of the star of propagation. For the purpose of the discussion we assume that measurements under magnetic field establish the structure shown in panel (d) as the solution for phase I of HoCu. Also shown in panel (d) is an extrapolation of the triple-k structure to inter-atomic positions in terms small arrows illustrating the director field. One unit cell may be viewed as a monopole–antimonopole pair denoted by a red and a blue sphere at $a(3/4, 3/4, 3/4)$ and $a(1/4, 1/4, 1/4)$, respectively. Colors encode the flux of each arrow with respect to the nearest singularity. (e) Band structure calculated for the triple-k structure in terms of the minimal tight-binding model described in the text.

The Fourier description of a triple-k $(\pi\pi0)$ state such as t1 is given by

$$\boldsymbol{M}(\boldsymbol{R}) = M_0 \cdot \sum_{i=1}^{3} \hat{m}_i \cdot \cos(\boldsymbol{k}_i \cdot \boldsymbol{R}) \quad, \tag{2}$$

where $\boldsymbol{R}$ denotes the positions of the magnetic rare-earth ions. Decomposing t1 in terms of Fourier components given by $\hat{m}_1 = (0,1,0)$, $\hat{m}_2 = (0,0,1)$, and $\hat{m}_3 = (1,0,0)$, it may be seen that t1 resembles the monopole–antimonopole lattice reported in MnGe [15]. Extending the magnetization $\boldsymbol{M}(\boldsymbol{r})$ analytically to locations between rare-earth lattice sites, singularities are located at the positions $\boldsymbol{r} = \frac{1}{4}(a,a,a)$ and $\frac{3}{4}(a,a,a)$ where the magnetization vanishes and the Berry curvature $b_l = \frac{1}{2}\epsilon^{ijl}\boldsymbol{n} \cdot [\partial_i\boldsymbol{n} \times \partial_j\boldsymbol{n}]$ derived from the director field $\boldsymbol{n} = \boldsymbol{M}/|\boldsymbol{M}|$ is topologically non-trivial with effective magnetic charges given by $Q_M = \frac{1}{4\pi}\int_S \mathrm{d}S_l \cdot b_l = \pm 1$, see [15]. In fact, around the same positions the directorfield forms a hedgehog and an antihedgehog, respectively. While a real-space interpretation of phase I based on a continuous magnetization field suggesting microscopic monopoles and anti-monopoles is intriguing, it must also be emphasized that it is inconsistent with a bare magnetic structure, $\boldsymbol{M}(\boldsymbol{R})$, composed of local moments, in which mirror and rotational symmetries must be broken to generate the interpolation $\boldsymbol{M}(\boldsymbol{r})$.

Shedding a different light on the topological properties of the triple-k structure t1, it is also instructive to consider the associated band structure on the level of a minimal tight-binding model given by [23]

$$H = \sum_{\langle i,j \rangle} t_{ij} c_i^\dagger c_j + J_H \sum_i \boldsymbol{\sigma} \cdot \boldsymbol{S}_i c_i^\dagger c_i \quad, \tag{3}$$

where $c_i^\dagger$ and c_i represent the two-component creation and annihilation operators of an electron at site i. The first term describes hopping between low-order nearest neighbors and the second term describes the coupling between conduction electrons and the magnetic structure treated as local exchange field $\boldsymbol{S}_i$. In the limit of fully polarized localized moments, i.e., $J_H \rightarrow \infty$, a spinless tight-binding model is obtained with hopping parameters $t_{ij}^{\text{eff}} = t_{ij} \cdot \langle \chi_i | \chi_j \rangle$, where

$$|\chi_i\rangle := [\cos(\theta_i/2), \sin(\theta_i/2) \cdot \exp(\mathrm{i}\cdot\Phi_i)]^{\mathrm{T}} \tag{4}$$

represents a spinor describing a classical spin $\boldsymbol{S}_i$ in terms of spherical angles θ_i and Φ_i [23]. Solving this model in the absence of spin–orbit coupling for a typical set of parameters given by $t_{\langle 100\rangle} = t_{\langle 110\rangle} = t$, the band structure displays Berry curvature with a rich distribution of positive and negative magnetic charges in reciprocal space [81]. Figure 6(e) shows the resulting band structure at momentum $k_z = \frac{\pi}{2a}$, where four singularities of quantized charges emerge.
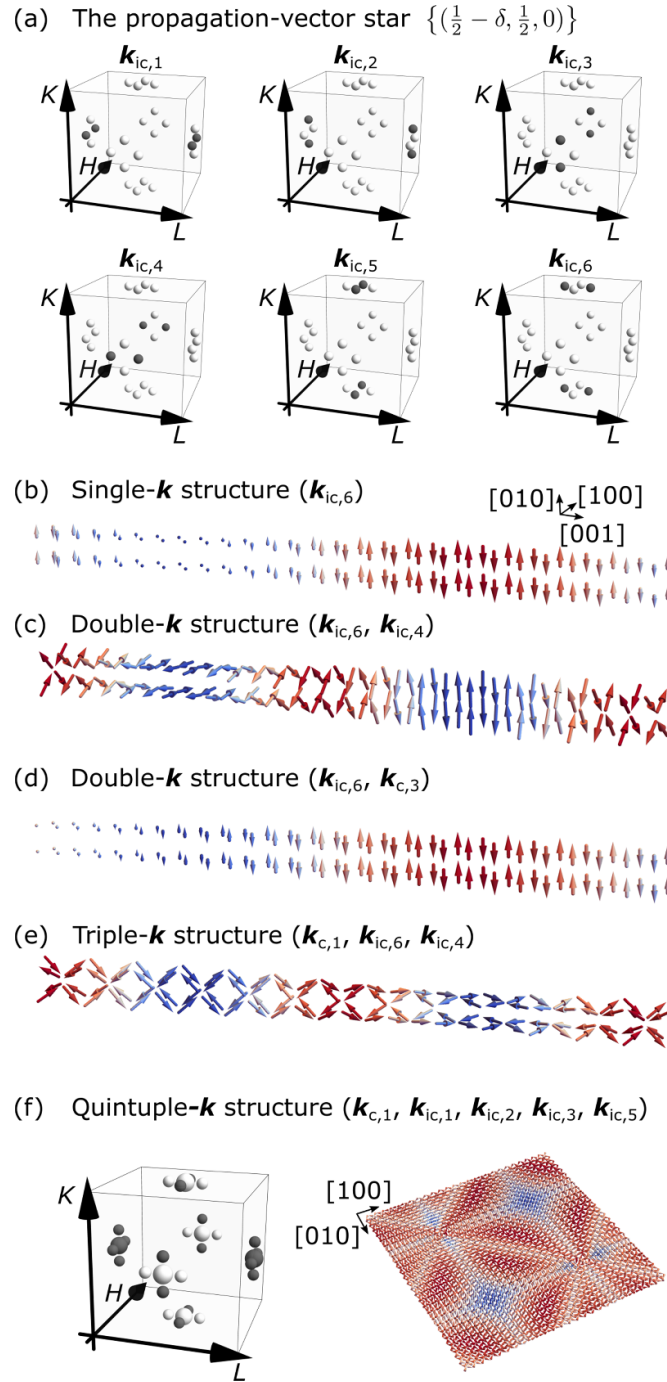
Figure 7. Considerations motivated by the magnetic structure observed in phase II of HoCu. (a) The magnetic ground state is a superposition of wave vectors from the stars $\left\{\left(\frac{1}{2}-\delta,\frac{1}{2},0\right)\right\}$ and $\left\{\left(\frac{1}{2},\frac{1}{2},0\right)\right\}$. The latter yields six arms that are here illustrated by the positions in the Brillouin zone. (b) Bare modulation of a single incommensurate wave vector representing an amplitude modulation. (c) Exemplary phase-shifted superposition of two such amplitude modulations resulting in a non-chiral helix. (d) Collinear double-*k* structure resulting from one commensurate and one incommensurate propagation vector. (e) Four-sublattice non-chiral cone structure resulting from a superposition of two incommensurate and one commensurate propagation vectors and identified by us as the magnetic structure in phase II. (f) Four-sublattice antiferromagnetic skyrmion lattice resulting from a superposition of four incommensurate and one commensurate propagation vectors.

The minimal tight-binding model and the resulting assembly of charges creating Berry curvatures permit to discuss the properties of the triple-*k* structure t1 further. For instance, in the presence of an anisotropic distortion of the lattice with respect to the [111] direction, a displacement of

the charges causing the Berry curvatures are expected resulting in two-dimensional Chern numbers, a finite intrinsic anomalous Hall effect [23], and orbital magnetization (a similar phenomenon was studied in [82]). The latter may be calculated by means of the expression [83]

$$\mathbf{M}_{\text{orb}} = -\frac{\mathrm{i}e}{2\hbar} \sum_{n,\alpha} \int_{E_n < E_{\mathrm{F}}} \frac{\mathrm{d}^3 k}{(2\pi)^3} \left[\langle \partial_{\mathbf{k}} u_{n,\alpha} | \times (H - E_n) | \partial_{\mathbf{k}} u_{n,\alpha} \rangle \right.$$
$$\left. + 2 (E_n - E_F) \langle \partial_{\mathbf{k}} u_{n,\alpha} | \times | \partial_{\mathbf{k}} u_{n,\alpha} \rangle \right] \quad , \tag{5}$$

where H is a tight-binding Hamiltonian in momentum space, $|u_{n,\alpha}\rangle$ are Bloch waves with components α attributed to the antiferromagnetic sublattices, E_n denotes the energy of band n, and E_{F} denotes the Fermi energy. The distortion of the lattice is taken into account in terms of a slight change of hopping parameters for next-nearest neighbor bonds perpendicular to [111]. Finally, for the two domains of the triple-*k* structure, the orbital magnetization exhibits opposing direction and hence different Zeeman energies under an applied magnetic field. Accordingly, already on the level of this minimal model an anomalous response to an applied magnetic field may be expected.

3.2. Phase II of HoCu: incommensurate order

In the following, we assume that the magnetic state associated with phase II of HoCu comprises a combination of commensurate and incommensurate modulations that correspond to the irreducible representations Γ_3 and Γ_4 of the wave-vector stars $\langle 1/2, 1/2, 0 \rangle$ and $\{(1/2 - \delta, 1/2, 0)\}$, respectively. This assumption implies that magnetic moments associated with each wave-vector are directed along the ferromagnetically coupled $\langle 100 \rangle$ bond of the respective propagation. The star of incommensurate propagation vectors has six wave-vector arms as illustrated in figure 7(a). Since the three arms of commensurate wave-vectors must also be taken into account, the magnetic structure in phase II may be a multi-*k* structure with up to nine magnetic propagation vectors.

The bare modulation associated with a single incommensurate *k* vector of the associated irreducible representation corresponds to an amplitude modulation, as shown in figure 7(b). Such a magnetic state has been reported in HoAg and TmAg [53]. The superposition of such incommensurate wave vectors with a specific, well-defined phase relation may result in highly non-trivial magnetic textures, such as the four-sublattice non-chiral helix presented in figure 7(c). The latter arises from the $\pi/2$-shifted superposition of two amplitude modulations that are incommensurate along the same $\langle 100 \rangle$ direction. The simplest possible structure arising from the superposition of commensurate and incommensurate wave vectors and, according solely to irreducible representations, a candidate structure for phase II of HoCu is the collinear structure shown in figure 7(d), which was previously proposed to exist in ErCu and TmCu [50].

Structures with topologically non-trivial properties may emerge when more than one incommensurate modulation are involved. Presented in figure 7(e) is the triple-*k* structure that we identified as the most plausible magnetic solution of phase II. It represents a four-sublattice antiferromagnetic non-chiral cone. Notably, the latter displays a constant modulus of magnetic moments, which in general is favorable for *f*-electron moments. The modulation of the real-space texture changes

from coplanar to noncoplanar arrangements and the rotation associated with the superstructure follows the parametrization of a staggered parameter making a full winding in the real projective space $\mathbb{R}P^1$ over a real-space distance of $\sim \frac{1}{2} \cdot a/\delta = 9$ nm, which is half of the periodicity of the cones on each sublattice.

Shown in figure 7(f) is a quintuple-*k* structure, which arises from a superposition of one commensurate and four incommensurate propagation vectors and represents another possible solution consistent with the irreducible representations we assumed for phase II. Illustrated on the left-hand side of figure 7(f) is the expected diffraction intensity distribution of a single domain. The associated real-space texture represents a four-sublattice antiferromagnetic skyrmion lattice, in which half of the sublattices display positive winding numbers and the other half negative winding numbers. Starting from this configuration, the superposition of a sufficiently large uniform magnetization as induced by an applied magnetic field may stabilize a four-sublattice skyrmion state with equal winding numbers on each sublattice. The latter may give rise to complex transport properties, such as net Berry phases resulting in transverse resistivity emerging from intra-sublattice conduction processes.

4. Conclusions

In summary, we presented a short review of antiferromagnetic multi-*k* states in the cubic rare-earth copper compounds with special emphasis on their putative topological character. To illustrate the possible existence of topological textures in this materials system, we reported selected results in HoCu, ErCu, and TmCu, representing promising materials that may host topological antiferromagnetic order. In all compounds measurements of the magnetic susceptibility establish multi-pocketed magnetic phase diagrams characteristic of delicately balanced competing interactions. The electrical transport properties exhibit exceptionally large anomalous contributions in the resistivity and Hall effect that are strongly suggestive of non-trivial topological winding of the electronic and magnetic structure. Neutron scattering reveals variations of $(\pi\pi0)$ antiferromagnetic order throughout the magnetic phase diagrams, where some of the phases support multi-*k* states.

Assuming commensurate $(\pi\pi0)$ order consistent with experiment in HoCu, this structure represents a platform for topological band structures comprising monopoles and antimonopoles. On a related note, incommensurate superstructures of the $(\pi\pi0)$ antiferromagnetism consistent with phase II of HoCu may provide an example of an antiferromagnetic skyrmion lattice with non-vanishing topological winding in real space. This combination of properties reflecting opposing limits connects emerging topological properties in real and reciprocal space in a unprecedented way, extending the platform of materials properties currently studied in the context of spintronics, nano-electronics, as well as neuromorphic applications.

Data availability statement

Acknowledgments

Conflicts of interest

The authors declare no conflicts of interests.

ORCID iDs

W Simeth https://orcid.org/0000-0001-9890-1816
M C Rahn https://orcid.org/0000-0001-7403-8288
A Bauer https://orcid.org/0000-0002-1070-9748
M Meven https://orcid.org/0000-0002-8079-5848
C Pfleiderer https://orcid.org/0000-0001-7749-7965

References

[1] Christensen D V *et al* 2022 2022 roadmap on neuromorphic computing and engineering *Neuromorph. Comput. Eng.* **2** 022501
[2] Singh P K, Singh Y, Chhabra J K, Illés Z and Verma C (eds) 2022 *Recent Innovations in Computing: Proc. ICRIC 2021, Volume 2* vol 855 (Springer)
[3] Marković D, Mizrahi A, Querlioz D and Grollier J 2020 Physics for neuromorphic computing *Nat. Rev. Phys.* **2** 499
[4] Grollier J, Querlioz D, Camsari K Y, Everschor-Sitte K, Fukami S and Stiles M D 2020 Neuromorphic spintronics *Nat. Electron.* **3** 360
[5] Song K M *et al* 2020 Skyrmion-based artificial synapses for neuromorphic computing *Nat. Electron.* **3** 148
[6] Mahmoud A, Ciubotaru F, Vanderveken F, Chumak A V, Hamdioui S, Adelmann C and Cotofana S 2020 Introduction to spin wave computing *J. Appl. Phys.* **128** 161101
[7] Hoffmann A *et al* 2022 Quantum materials for energy-efficient neuromorphic computing *APL Mater.* **10** 070904
[8] Bak P and Lebech B 1978 'Triple-$\vec{q}$' modulated magnetic structure and critical behavior of neodymium *Phys. Rev. Lett.* **40** 800
[9] Shapiro S M, Gurewitz E, Parks R D and Kupferberg L C 1979 Multiple-q magnetic structure in $CeAl_2$ *Phys. Rev. Lett.* **43** 1748
[10] Back C *et al* 2020 The 2020 skyrmionics roadmap *J. Phys. D: Appl. Phys.* **53** 363001
[11] Mühlbauer S, Binz B, Jonietz F, Pfleiderer C, Rosch A, Neubauer A, Georgii R and Böni P 2009 Skyrmion lattice in a chiral magnet *Science* **323** 915–9
[12] Khanh N D *et al* 2020 Nanometric square skyrmion lattice in a centrosymmetric tetragonal magnet *Nat. Nanotechnol.* **15** 444
[13] Yu X Z, Koshibae W, Tokunaga Y, Shibata K, Taguchi Y, Nagaosa N and Tokura Y 2018 Transformation between meron and skyrmion topological spin textures in a chiral magnet *Nature* **564** 95
[14] Puphal P *et al* 2020 Topological magnetic phase in the candidate Weyl semimetal CeAlGe *Phys. Rev. Lett.* **124** 017202
[15] Kanazawa N, Nii Y, Zhang X-X, Mishchenko A S, De Filippis G, Kagawa F, Iwasa Y, Nagaosa N and Tokura Y 2016 Critical phenomena of emergent magnetic monopoles in a chiral magnet *Nat. Commun.* **7** 11622
[16] Gao S *et al* 2020 Fractional antiferromagnetic skyrmion lattice induced by anisotropic couplings *Nature* **586** 37
[17] Chacon A, Heinen L, Halder M, Bauer A, Simeth W, Mühlbauer S, Berger H, Garst M, Rosch A and Pfleiderer C 2018 Observation of two independent skyrmion phases in a chiral magnetic material *Nat. Phys.* **14** 936
[18] Halder M, Chacon A, Bauer A, Simeth W, Mühlbauer S, Berger H, Heinen L, Garst M, Rosch A and Pfleiderer C 2018 Thermodynamic evidence of a second skyrmion lattice phase and tilted conical phase in Cu_2OSeO_3 *Phys. Rev. B* **98** 144429
[19] Aqeel A, Sahliger J, Taniguchi T, Mändl S, Mettus D, Berger H, Bauer A, Garst M, Pfleiderer C and Back C H 2021 Microwave spectroscopy of the low-temperature skyrmion state in Cu_2OSeO_3 *Phys. Rev. Lett.* **126** 017202
[20] Kezsmarki I *et al* 2015 Néel-type skyrmion lattice with confined orientation in the polar magnetic semiconductor GaV_4S_8 *Nat. Mater.* **14** 1116
[21] Kurumaji T, Nakajima T, Hirschberger M, Kikkawa A, Yamasaki Y, Sagayama H, Nakao H, Taguchi Y, Arima T-hisa and Tokura Y 2019 Skyrmion lattice with a giant topological Hall effect in a frustrated triangular-lattice magnet *Science* **365** 914
[22] Hirschberger M *et al* 2019 Skyrmion phase and competing magnetic orders on a breathing kagomé lattice *Nat. Commun.* **10** 5831
[23] Nagaosa N, Sinova J, Onoda S, MacDonald A H and Ong N P 2010 Anomalous Hall effect *Rev. Mod. Phys.* **82** 1539
[24] Neubauer A, Pfleiderer C, Binz B, Rosch A, Ritz R, Niklowitz P G and Böni P 2009 Topological Hall effect in the *A* phase of MnSi *Phys. Rev. Lett.* **102** 186602
[25] Yasui Y *et al* 2020 Imaging the coupling between itinerant electrons and localised moments in the centrosymmetric skyrmion magnet $GdRu_2Si_2$ *Nat. Commun.* **11** 5925
[26] Buschow K 1977 Intermetallic compounds of rare-earth and 3d transition metals *Rep. Prog. Phys.* **40** 1179
[27] Buschow K 1979 Intermetallic compounds of rare earths and non-magnetic metals *Rep. Prog. Phys.* **42** 1373

[28] Rossat-Mignod J 1979 Magnetic structures of rare earth intermetallics *J. Phys. Colloq.* **40** C5

[29] Szytuła A and Leciejewicz J 1989 Magnetic properties of ternary intermetallic compounds of the RT_2X_2 type *Handbook on the Physics and Chemistry of Rare Earths* vol 12 (Elsevier) ch 83, p 133

[30] Gignoux D and Schmitt D 1997 Magnetism of compounds of rare earths with non-magnetic metals *Handbook of Magnetic Materials* vol 10 (Elsevier) ch 2, p 239

[31] Jensen J and Mackintosh A R 1991 *Rare Earth Magnetism* (Clarendon)

[32] Ruderman M A and Kittel C 1954 Indirect exchange coupling of nuclear magnetic moments by conduction electrons *Phys. Rev.* **96** 99

[33] Kasuya T 1956 A theory of metallic ferro- and antiferromagnetism on Zener's model *Prog. Theor. Phys.* **16** 45

[34] Yosida K 1957 Magnetic properties of Cu-Mn alloys *Phys. Rev.* **106** 893

[35] Amara M, Morin P and Burlet P 1995 Experimental study of the magnetic phase diagrams in NdZn *Physica* B **210** 157

[36] Morin P, Rouchy J, Yonenobu K, Yamagishi A and Date M 1989 Interplay of antiferromagnetic and antiferroquadrupolar interactions in DyAg and other rare earth intermetallic compounds *J. Magn. Magn. Mater.* **81** 247

[37] Morin P, Giraud M, Burlet P and Czopnik A 1987 Antiferroquadrupolar and antiferromagnetic structures in TmGa$_3$ *J. Magn. Magn. Mater.* **68** 107

[38] Rossat-Mignod J, Burlet P, Villain J, Bartholin H, Tcheng-Si W, Florence D and Vogt O 1977 Phase diagram and magnetic structures of CeSb *Phys. Rev.* B **16** 440

[39] Kakeya I, Kakeshita T, Kindo K, Yamamoto Y and Saburi T 1999 High field magnetization in DyCu *J. Phys. Soc. Japan* **68** 1025

[40] Amara M, Morin P and Bourdarot F 1997 Experimental study of the magnetic phase diagrams of DyCu *J. Phys.: Condens. Matter* **9** 7441

[41] Amara M, Galéra R M, Morin P, Voiron J and Burlet P 1994 Magnetic phase diagram in NdIn$_3$ antiferromagnet *J. Magn. Magn. Mater.* **131** 402

[42] Galéra R M, Sole E, Amara M, Morin P, Burlet P and Murani A P 2003 The interplay of the crystalline electric field and quadrupolar interactions in the spontaneous magnetic phases of DyIn$_3$ *J. Phys.: Condens. Matter* **15** 6269

[43] Morin P and Schmitt D 1982 Magnetic properties and quadrupolar interactions in PrAg *Phys. Rev.* B **26** 3891

[44] Givord D, Morin P and Schmitt D 1985 Study of antiferromagnetic structures by polarized neutrons: application to PrAg *J. Appl. Phys.* **57** 2127

[45] Buschow K H J, de Jong J P, Zandbergen H W and van Laar B 1975 Magnetic properties of some light rare-earth compounds with CsCl structure *J. Appl. Phys.* **46** 1352

[46] Cable J W, Koehler W C and Wollan E O 1964 Magnetic order in rare-earth intermetallic compounds *Phys. Rev.* **136** A240

[47] Arnold G, Nereson N and Olsen C 1967 Magnetic structure of DyAg *J. Chem. Phys.* **46** 4041

[48] Nereson N 1973 Magnetic properties of ErAg *J. Appl. Phys.* **44** 4727

[49] Blanco J A, Espeso J I, García Soldevilla J, Gómez Sal J C, Ibarra M R, Marquina C and Fischer H E 1999 Magnetic structure of GdCu through the martensitic structural transformation: a neutron-diffraction study *Phys. Rev.* B **59** 512

[50] Morin P and Schmitt D 1980 Competition between multi-*q* antiferromagnetic structures in cubic rare earth-copper compounds *J. Magn. Magn. Mater.* **21** 243

[51] Aléonard R, Morin P and Rouchy J 1984 Magnetic and quadrupolar properties of DyCu and related dysprosium cubic compounds *J. Magn. Magn. Mater.* **46** 233

[52] Yasui M, Terai T, Kakeshita T, Matsuda M, Metoki N and Nojiri H 2008 Neutron diffraction study of magnetic structure in DyCu under magnetic field *J. Appl. Phys.* **103** 07B710

[53] Morin P, Schmitt D and Vettier C 1985 Squaring-up of modulated magnetic structures in HoAg and TmAg *J. Physique* **46** 39

[54] Morin P, Giraud M, Burlet P and Czopnik A 1987 Antiferroquadrupolar and antiferromagnetic structures in TmGa$_3$ *J. Magn. Magn. Mater.* **68** 107

[55] Nereson N and Arnold G 1970 Magnetic properties of TbIn$_3$, TbPt$_3$ and HoIn$_3$ *J. Chem. Phys.* **53** 2818

[56] Murasik A, Czopnik A, Keller L and Fischer P 2000 Spin rotation in ErGa$_3$ *J. Magn. Magn. Mater.* **213** 101

[57] Morin P and Schmitt D 1990 Quadrupolar interactions and magneto-elastic effects in rare earth intermetallic compounds *Handbook of Ferromagnetic Materials* vol 5 (Elsevier) ch 1, p 1

[58] Rahn M 2013 Search for topological properties of multi-k magnetic structures *Diploma Thesis* Technical University of Munich (unpublished)

[59] Hautmann H 2013 Untersuchung des magnetischen Phasendiagramms von ErCu *Bachelor Thesis* Technical University of Munich (unpublished)

[60] Bonacic N 2016 Measurements of heat capacity of systems with complex magnetic phase diagrams for magnetic field along hard magnetisation axis *Master Thesis* University of Zagreb

[61] Simeth W 2019 Investigation of antiferromagnetic superstructures in rare-earth compounds *PhD Thesis* Technical University of Munich

[62] Neubauer A, Bœuf J, Bauer A, Russ B, Löhneysen H and Pfleiderer C 2011 Ultra-high vacuum compatible image furnace *Rev. Sci. Instrum.* **82** 013902

[63] Bauer A, Benka G, Regnat A, Franz C and Pfleiderer C 2016 Ultra-high vacuum compatible preparation chain for intermetallic compounds *Rev. Sci. Instrum.* **87** 113902

[64] Meven M and Sazonov A 2015 HEiDi: single crystal diffractometer at hot source *J. Large-Scale Res. Facil. JLSRF* **1** A7

[65] Su Y, Nemkovskiy K and Demirdiş S 2015 DNS: diffuse scattering neutron time-of-flight spectrometer *J. Large-Scale Res. Facil. JLSRF* **1** 27

[66] Georgii R, Weber T, Brandl G, Skoulatos M, Janoschek M, Mühlbauer S, Pfleiderer C and Böni P 2018 The multi-purpose three-axis spectrometer (TAS) MIRA at FRM II *Nucl. Instrum. Methods Phys. Res.* A **881** 60

[67] Chapon L C *et al* 2011 Wish: the new powder and single crystal magnetic diffractometer on the second target station *Neutron News* **22** 22

[68] Ostermann A and Schrader T 2015 BIODIFF: diffractometer for large unit cells *J. Large-Scale Res. Facil. JLSRF* **1** 2

[69] Heinemann A and Mühlbauer S 2015 SANS-1: small angle neutron scattering *J. Large-Scale Res. Facil. JLSRF* **1** 10

[70] Keen D A, Gutmann M J and Wilson C C 2006 SXD—the single-crystal diffractometer at the ISIS spallation neutron source *J. Appl. Crystallogr.* **39** 714

[71] Prokeš K and Yokoachiya F 2017 E4: the 2-axis diffractometer at BER II *J. Large-Scale Res. Facil. JLSRF* **3** 104

[72] Hutanu V 2015 POLI: polarised hot neutron diffractometer *J. Large-Scale Res. Facil. JLSRF* **1** 16

[73] Li Y-Y 1955 Magnetic moment arrangements and magnetocrystalline deformations in antiferromagnetic compounds *Phys. Rev.* **100** 627

[74] Shirane G 1959 A note on the magnetic intensities of powder neutron diffraction *Acta Crystallogr.* **12** 282

[75] Barbara B, Rossignol M F, Boucherle J X and Vettier C 1980 Multiple-$\vec{q}$ structure or coexistence of different magnetic phases in $CeAl_2$? *Phys. Rev. Lett.* **45** 938

[76] Forgan E M, Gibbons E P, McEwen K A and Fort D 1989 Observation of a quadruple-q magnetic structure in neodymium *Phys. Rev. Lett.* **62** 470

[77] Adams T *et al* 2011 Long-range crystalline nature of the skyrmion lattice in MnSi *Phys. Rev. Lett.* **107** 217206

[78] Wills A S 2000 A new protocol for the determination of magnetic structures using simulated annealing and representational analysis (SARAh) *Physica* B **276–278** 680

[79] Petříček V, Dušek M and Palatinus L 2014 Crystallographic computing system JANA2006: general features *Z. Kristallogr.* **229** 345–52

[80] Ishizuka H and Nagaosa N 2018 Spin chirality induced skew scattering and anomalous Hall effect in chiral magnets *Sci. Adv.* **4** eaa9962

[81] Xiao D, Shi J and Niu Q 2005 Berry phase correction to electron density of states in solids *Phys. Rev. Lett.* **95** 137204

[82] Shindou R and Nagaosa N 2001 Orbital ferromagnetism and anomalous Hall effect in antiferromagnets on the distorted fcc lattice *Phys. Rev. Lett.* **87** 116801

[83] Shi J, Vignale G, Xiao D and Niu Q 2007 Quantum theory of orbital magnetization and its generalization to interacting systems *Phys. Rev. Lett.* **99** 197202